International Conference on Mathematics, Computational Methods & Reactor Physics (M&C 2009)
Saratoga Springs, New York, May 3-7, 2009, on CD-ROM, American Nuclear Society, LaGrange Park, IL (2009)

A HYBRID MONTE CARLO-S_2 METHOD FOR PRESERVING NEUTRON TRANSPORT EFFECTS

Emily R. Wolters, Edward W. Larsen and William R. Martin
Department of Nuclear Engineering & Radiological Sciences
University of Michigan
2355 Bonisteel Boulevard, Ann Arbor, MI 48109
ewolters@umich.edu; edlarsen@umich.edu; wrm@umich.edu

ABSTRACT

A new hybrid method has been developed to efficiently and accurately solve neutron transport problems with significant transport effects. In particular, fast reactor core-reflector problems exhibit strong spectral effects near interfaces because of the coupled energy and directional dependence of the flux [1-4]. Deterministic methods may fail to solve these types of problems accurately because of the conventional multigroup approximation [1-6]. The proposed hybrid method is a combination of Monte Carlo and modified discrete ordinates calculations. To derive this method, we reduce the transport equation to "low-order" equations (one energy group, two direction groups) containing special nonlinear functionals rather than multigroup cross sections. These functionals are determined by continuous-energy Monte Carlo. The "low-order" equations are exact except for small statistical errors in the functionals and a small spatial truncation error. Given exact values of the functionals, the low-order equations have no energy or angular truncation errors. For a meaningful test problem, the hybrid method is significantly more accurate than multigroup discrete ordinates calculations for calculating scalar flux and reaction rates. Also, the hybrid method solution has a significantly higher figure of merit than a standard Monte Carlo solution.

Key Words: hybrid, transport effect, interface, multigroup, Monte Carlo

1. INTRODUCTION

Researchers have encountered difficulties using deterministic methods to solve neutron transport problems with significant transport effects [1-4]. For example, at material interfaces, the neutron angular flux may exhibit a strong correlation between energy and angle. This effect is difficult to capture using conventional deterministic methods because of the many approximations required to reduce the exact transport equation to a set of linear equations solvable on a computer. It is important to address these issues because candidate future reactors such as the Very High Temperature Reactor (VHTR) and the Advanced Burner Reactor (ABR) may exhibit these effects.

The motivation for this work was the analysis done by Aliberti, et al [1] and Lebrat, et al [2], who considered a model reflected fast reactor, consisting of a cylindrical fast core surrounded by a reflector material. Near the core-reflector interface, the direction of a neutron is strongly correlated to its energy, as most neutrons leaving the core are faster than those entering the core from the reflector. This correlation causes a significant spectral effect near the interface. Aliberti and Lebrat attempted to calculate reaction rates near the core-reflector interface and the

eigenvalue for this problem using conventional deterministic methods. They found that satisfactory results could be achieved only by using a very large number of energy groups (G=300). They developed an improved broad group (G=33) methodology by subdividing the core and reflector into multiple spatial regions and calculating the true spectral weighting function in a coupled core-reflector calculation to obtain more accurate, spatially dependent cross sections. Other authors also noted the importance of spectral differences near interfaces [3,4] and recommended the generation of spatially dependent spectra for multigroup cross section collapsing. However, these techniques do not directly address the root of the problem.

The multigroup approximation is the primary cause of the observed deterministic method failure. We recall that the rigorous multigroup cross section definition preserves reaction rates by weighting the continuous-energy cross section with the angular flux, i.e.,

$$\Sigma_{t,g}\left(\vec{r},\hat{\Omega}\right)\equiv\frac{\int_{E_g}^{E_{g-1}}\Sigma_t\left(\vec{r},E\right)\psi\left(\vec{r},\hat{\Omega},E\right)}{\int_{E_g}^{E_{g-1}}\psi\left(\vec{r},\hat{\Omega},E\right)}. \tag{1}$$

However, the angular dependence of the resulting multigroup cross section cannot be incorporated into a conventional deterministic code framework. In practice, the angular flux weighting function is replaced with one which is separable in angle and energy, and independent of space:

$$\Sigma_{t,g}^{i}=\frac{\int_{E_g}^{E_{g-1}}dE\Sigma_t^i\left(E\right)\Psi^i\left(E\right)}{\int_{E_g}^{E_{g-1}}dE\Psi^i\left(E\right)}. \tag{2}$$

For problems with significant transport effects, the multigroup cross section does not always preserve reaction rates. Hanshaw [5,6] developed an adjoint weighting function which improves results for problems with strong spatial and angular variation. However, this method still approximates Eq. (1).

In this paper we develop an accurate hybrid (Monte Carlo – deterministic) method for problems with neutron transport effects. Our method does not use the multigroup approximation; rather, it utilizes special functionals that incorporate energy, direction, and spatial information.

2. THE HYBRID METHOD

We consider the 1-D neutron transport equation with boundary conditions,

$$\mu\frac{\partial}{\partial x}\psi\left(x,\mu,E\right)+\Sigma_t\left(x,E\right)\psi\left(x,\mu,E\right)=\frac{1}{2}\int_0^\infty dE'\Sigma_s\left(x,E'\right)p(x,E'\to E)\phi\left(x,E'\right)+\frac{1}{2}Q\left(x,E\right) \tag{3}$$

$$\psi\left(0,\mu,E\right)=\psi\left(0,-\mu,E\right),\quad 0<\mu\le 1,\quad 0<E<\infty \tag{4}$$

$$\psi\left(b,\mu,E\right)=0,\quad -1\le\mu<0,\quad 0<E<\infty\,. \tag{5}$$

For simplicity, we assume no fission, inelastic scattering, or upscatter, and elastic scattering is assumed to be isotropic. The elastic scattering kernel is proportional to

$$p\left(x,E'\to E\right)=\begin{cases}\dfrac{1}{\left(1-\alpha\left(x\right)\right)E'}, & \alpha\left(x\right)E'<E<E'\\ 0, & otherwise\end{cases}, \tag{6}$$

where $\alpha\left(x\right)=\left(\dfrac{A\left(x\right)-1}{A\left(x\right)+1}\right)^2$. Again for simplicity, the source is assumed to be isotropic.

We would like to compute reaction rates $F_i\left(x\right)$ throughout the system,

$$F_i\left(x\right)=\int_0^\infty dEf_i\left(x,E\right)\phi\left(x,E\right) \tag{7}$$

These reaction rates must be chosen *a priori*, but an arbitrary number of them may be chosen.

2.1. Derivation of the Functional Equations

We begin with the exact transport equation and boundary conditions in Eqs. (3)-(5), and a single function $f\left(x,E\right)$ in Eq. (7). We define the "half-range" scalar fluxes (per unit energy)

$$\psi^{\pm}\left(x,E\right)\equiv\pm\int_0^{\pm1}d\mu\psi\left(x,\mu,E\right). \tag{8}$$

The desired reaction rate can be written as

$$F\left(x\right)=\int_0^\infty dEf\left(x,E\right)\left[\psi^{+}\left(x,E\right)+\psi^{-}\left(x,E\right)\right]=F^{+}\left(x\right)+F^{-}\left(x\right), \tag{9}$$

where

$$F^{\pm}\left(x\right)\equiv\int_0^\infty dEf\left(x,E\right)\psi^{\pm}\left(x,E\right). \tag{10}$$

To derive equations for $F^{\pm}\left(x\right)$, we do the following.

Step 1. Operate on Eq. (3) by $\int_0^\infty dE\left(\cdot\right)$ and use $\int_0^\infty dEp\left(x,E'\to E\right)=1$.

Step 2. Operate on the result of Step 1 separately by $\int_0^1 d\mu\left(\cdot\right)$ and $\int_{-1}^0 d\mu\left(\cdot\right)$.

Step 3. Introduce a spatial mesh, $\left\{x_{j+1/2},\quad j=0,J\right\}$ which covers the entire range of the geometry and whose points lie at material interfaces, boundaries and anywhere in

between. The j[th] cell has width $\Delta x_j = x_{j+1/2} - x_{j-1/2}$. Operate on both results of Step 2 by $\frac{1}{\Delta x_j}\int_{x_{j-1/2}}^{x_{j+1.2}} dx(\cdot)$.

Step 4. Simplify the leakage term by evaluating the integrals of perfect differentials.
Step 5. Multiply and divide each term by convenient factors of unity (shown below).

The result of these steps is (only integration for positive polar cosine shown)

$$\frac{1}{\Delta x_j}\left\{\left[\frac{\int_0^\infty dE\int_0^1 d\mu\,\mu\psi\left(x_{j+1/2},\mu,E\right)}{F^+\left(x_{j+1/2}\right)}\right]F^+\left(x_{j+1/2}\right)-\left[\frac{\int_0^\infty dE\int_0^1 d\mu\,\mu\psi\left(x_{j-1/2},\mu,E\right)}{F^+\left(x_{j-1/2}\right)}\right]F^+\left(x_{j-1/2}\right)\right\}$$
$$+\frac{1}{\Delta x_j}\left[\frac{\int_{x_{j-1/2}}^{x_{j+1/2}} dx\int_0^\infty dE\Sigma_t\left(x,E\right)\psi^+\left(x,E\right)}{\int_{x_{j-1/2}}^{x_{j+1/2}} dxF^+\left(x\right)}\right]\int_{x_{j-1/2}}^{x_{j+1/2}} dxF^+\left(x\right)$$
$$=\frac{1}{2}\frac{1}{\Delta x_j}\left[\frac{\int_{x_{j-1/2}}^{x_{j+1/2}} dx\int_0^\infty dE'\Sigma_s\left(x,E'\right)\psi^+\left(x,E'\right)}{\int_{x_{j-1/2}}^{x_{j+1/2}} dxF^+\left(x\right)}\right]\int_{x_{j-1/2}}^{x_{j+1/2}} dxF^+\left(x\right) \qquad (11)$$
$$+\frac{1}{2}\frac{1}{\Delta x_j}\left[\frac{\int_{x_{j-1/2}}^{x_{j+1/2}} dx\int_0^\infty dE'\Sigma_s\left(x,E'\right)\psi^-\left(x,E'\right)}{\int_{x_{j-1/2}}^{x_{j+1/2}} dxF^-\left(x\right)}\right]\int_{x_{j-1/2}}^{x_{j+1/2}} dxF^-\left(x\right)$$
$$+\frac{1}{2}\frac{1}{\Delta x_j}\int_{x_{j-1/2}}^{x_{j+1/2}} dx\int_0^\infty dEQ\left(x,E\right), \qquad j=1,\ldots J.$$

We define each of the above bracketed terms as the following "functionals":

$$\mu_{j+1/2}^{\pm} \equiv \frac{\pm\int_0^\infty dE\int_0^{\pm1} d\mu\,\mu\psi\left(x_{j+1/2},\mu,E\right)}{F^{\pm}\left(x_{j+1/2}\right)} = \frac{\pm\int_0^\infty dE\int_0^{\pm1} d\mu\,\mu\psi\left(x_{j+1/2},\mu,E\right)}{\pm\int_0^\infty dE\int_0^{\pm1} d\mu\, f\left(x_{j+1/2},E\right)\psi\left(x_{j+1/2},\mu,E\right)} = \frac{J_{j+1/2}^{\pm}}{F_{j+1/2}^{\pm}} \qquad (12)$$
$$j=0,\ldots J,$$

$$\Sigma_{i,j}^{\pm} \equiv \frac{\int_{x_{j-1/2}}^{x_{j+1/2}} dx\int_0^\infty dE\Sigma_i\left(x,E\right)\psi^{\pm}\left(x,E\right)}{\int_{x_{j-1/2}}^{x_{j+1/2}} dxF^{\pm}\left(x\right)} = \frac{\pm\int_{x_{j-1/2}}^{x_{j+1/2}} dx\int_0^\infty dE\int_0^{\pm1} d\mu\Sigma_i\left(x,E\right)\psi\left(x,\mu,E\right)}{\pm\int_{x_{j-1/2}}^{x_{j+1/2}} dx\int_0^\infty dE\int_0^{\pm1} d\mu\, f\left(x,E\right)\psi\left(x,\mu,E\right)} = \frac{Z_{i,j}^{\pm}}{F_j^{\pm}} \qquad (13)$$
$$i=\{s,t\} \quad j=1,\ldots J.$$

We also define:

$$Q_j \equiv \frac{1}{\Delta x_j}\int_{x_{j-1/2}}^{x_{j+1/2}} dx Q(x), \tag{14}$$

$$F_j^{\pm} \equiv \frac{1}{\Delta x_j}\int_{x_{j-1/2}}^{x_{j+1/2}} dx F^{\pm}(x), \tag{15}$$

$$F_{j+1/2}^{\pm} = F^{\pm}\left(x_{j+1/2}\right). \tag{16}$$

Using these definitions, Eq. (11) can be written:

$$\frac{1}{\Delta x_j}\left[\mu_{j+1/2}^{+}F_{j+1/2}^{+} - \mu_{j-1/2}^{+}F_{j-1/2}^{+}\right] + \Sigma_{t,j}^{+}F_j^{+} = \frac{1}{2}\Sigma_{s,j}^{+}F_j^{+} + \frac{1}{2}\Sigma_{s,j}^{-}F_j^{-} + \frac{1}{2}Q_j. \tag{17}$$

A corresponding equation for the integration over negative polar cosine is not shown. This equation and Eq. (17) are exact equations for the cell boundary values of $F\left(x\right), F_{j+1/2}^{\pm}$, and the cell averaged values of $F\left(x\right), F_j^{\pm}$. To reduce the number of unknowns, we introduce a diamond difference approximation relating the boundary unknowns to the volume unknowns,

$$F_j^{\pm} = \frac{1}{2}\left(F_{j+1/2}^{\pm} + F_{j-1/2}^{\pm}\right). \tag{18}$$

This results in the following set of S_2-like equations:

$$\begin{aligned}
&\frac{1}{\Delta x_j}\left[\mu_{j+1/2}^{+}F_{j+1/2}^{+} - \mu_{j-1/2}^{+}F_{j-1/2}^{+}\right] + \frac{\Sigma_{t,j}^{+}}{2}\left(F_{j+1/2}^{+} + F_{j-1/2}^{+}\right) = S_j^{+} \\
&\frac{1}{\Delta x_j}\left[\mu_{j+1/2}^{-}F_{j+1/2}^{-} - \mu_{j-1/2}^{-}F_{j-1/2}^{-}\right] + \frac{\Sigma_{t,j}^{-}}{2}\left(F_{j+1/2}^{-} + F_{j-1/2}^{-}\right) = S_j^{-}
\end{aligned} \tag{19}$$

$$S_j^{\pm} = \frac{1}{2}\Sigma_{s,j}^{+}F_j^{+} + \frac{1}{2}\Sigma_{s,j}^{-}F_j^{-} + \frac{1}{2}Q_j \tag{20}$$

$$F_{1/2}^{+} = F_{1/2}^{-}, \quad F_{J+1/2}^{-} = 0, \quad j = 1,\ldots J. \tag{21}$$

Eqs. (8)-(21) constitute a completely specified low-order problem for the boundary and volume-averaged values of $F^{\pm}\left(x\right)$, assuming that the functionals $\mu_{j+1/2}^{\pm}, \Sigma_{t,j}^{\pm}$ and $\Sigma_{s,j}^{\pm}$ are known. The equations are *exact* in energy and angle; the only approximation made was the spatial diamond difference relation in (18). We refer to these equations as the "functional discrete ordinates" equations because they are easily solved using a discrete ordinates-like transport sweep and source iteration. Prior to solving, however, we must compute the functionals, which are dependent on the unknown angular flux. We would like to note that the low-order equations bear

resemblance to work by Roberts and Anistratov [7], but that work was fundamentally different from our approach.

2.2. Monte Carlo Computation of the Functionals

To compute the functionals defined in Eqs. (12) and (13), we simulate the exact problem, including the correct spatial mesh, in Monte Carlo and tally the integrals in Eqs. (12) and (13). Taking ratios of these integrals yields the desired functionals.

One may question the strategy of using Monte Carlo to estimate the functionals in Eqs. (12) and (13) instead of the desired reaction rates. Our strategy is based on the following fundamental hypothesis:

> *Hypothesis:* Monte Carlo estimates of the nonlinear functionals in Eqs. (12) and (13) are much more accurate, and have much less variance, than direct Monte Carlo estimates of the desired reaction rates.

This hypothesis is based on the observation that Monte Carlo estimates of the functionals are *weakly*-dependent on the number of Monte Carlo particles used to determine estimates, while direct Monte Carlo estimates of the reaction rates depend *strongly* on these numbers. Our numerical results (Sec. 4.1) confirm the basic truth of this hypothesis.

2.2.1. Cell volume-averaged functionals

Computation of the volume-averaged functionals $\Sigma_{s,j}^{\pm}$ and $\Sigma_{t,j}^{\pm}$ [defined in Eq. (13)] is straightforward. We require three modified path length estimator tallies: two for the numerators $Z_{s,j}^{\pm}$ and $Z_{t,j}^{\pm}$, and one for $F_j^{\pm}$.

2.2.2. Cell boundary functionals

The functionals $\mu_{j+1/2}^{\pm}$ [defined in Eq. (12)] lie on a cell boundary and consist of a numerator current tally, $J_{j+1/2}^{\pm}$ and a denominator modified surface flux estimator, $F_{j+1/2}^{\pm}$. To avoid the high variance of the $F_{j+1/2}^{\pm}$ tallies, we approximate the denominator with the neighboring cell-average tallies,

$$F_{j+1/2}^{\pm} \approx G_{j+1/2}^{\pm}, \tag{22}$$

where

$$G_{j+1/2}^{\pm} = \begin{cases} \frac{1}{2}\left(F_{j+1}^{+} + F_{j+1}^{-}\right) & j = 0 \\ \frac{1}{\Delta x_j + \Delta x_{j+1}}\left(\Delta x_{j+1} F_j^{\pm} + \Delta x_j F_{j+1}^{\pm}\right) & j = 1,\ldots J-1 \\ F_j^{\pm} & j = J. \end{cases} \tag{23}$$

The approximation at $j = 0$ preserves a reflecting boundary. The error introduced by Eq. (22) is negligible compared to the statistical noise which would have been introduced by the surface flux estimator, and is comparable to the truncation error introduced by Eq. (18).

2.3. Computation of Multiple Reaction Rates

To compute a single reaction rate, one Monte Carlo calculation is performed with four tallies ($Z^{\pm}_{s,j}$, $Z^{\pm}_{t,j}$, $J^{\pm}_{j+1/2}$ and $F^{\pm}_{j}$) to compute the set of functionals, which is then input to a modified discrete ordinates calculation.

To compute *n* reaction rates, one Monte Carlo calculation is performed with $3+n$ tallies to compute *n* sets of functionals. Each set of functionals is input to a separate modified discrete ordinates calculation.

Since the cost of the Monte Carlo calculation is usually dominated by geometry tracking, additional tallies do not increase the computational cost significantly. These additional tallies would also be required if using standard Monte Carlo as opposed to the hybrid method. Also, since the modified discrete ordinates calculation is low-order (one energy group, two direction groups), the additional computer time required for the multiple deterministic calculations is negligible compared to the time required for the Monte Carlo calculation.

2.4. Computation of Group Reaction Rates

There are two methods to obtain group reaction rates with the hybrid method. The first and simpler method (used in this work) is to assign

$$f_g(x,E) = \begin{cases} f(x,E), & E \in E_g \\ 0, & E \notin E_g. \end{cases} \tag{24}$$

This assignment gives the reaction rate

$$F_g(x) = \int_{\Delta E_g} dE f(x,E)\phi(x,E). \tag{25}$$

The second method, which will be explored in future work, is to integrate the transport equation over energy groups instead of the entire energy space. This would result in low-order equations resembling multigroup equations but having no approximation in energy or angle.

3. TEST PROBLEM DESCRIPTION

We consider the test problem in Fig. 1. The cross sections in the core and reflector are histogram approximations to Fe-56 and Na-23, respectively (see Appendix). An isotropic, mono-energetic (10 keV) source is spatially uniform in the core region.

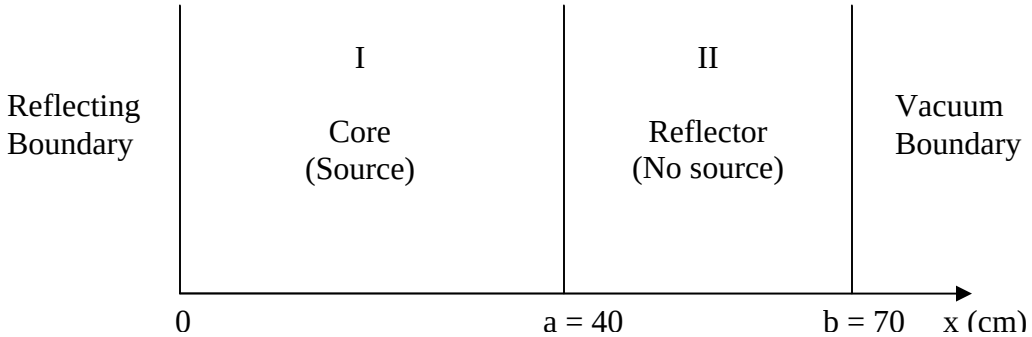

Figure 1. Slab geometry test problem.

We wish to compute the energy-integrated scalar flux and the capture rate. We therefore choose $f_1(x,E)=1$ and $f_2(x,E)=\Sigma_\gamma(x,E)$, so that $F_1(x)$ is the scalar flux and $F_2(x)$ is the capture rate.

4. HYBRID METHOD NUMERICAL RESULTS

In this section we compare the statistical properties of the hybrid method to that of Monte Carlo, and we compare the accuracy of the hybrid method to conventional deterministic methods for the test problem.

4.1. Comparison with Standard Monte Carlo

The variance of a standard Monte Carlo solution may be directly computed during the simulation, but the variance of the hybrid solution may only be estimated due to complexities in calculating the covariance of the functionals in the stochastic step and propagation of statistical error in the deterministic step.

To compare the two methods, twenty independent estimates of the scalar flux were obtained with standard Monte Carlo, and twenty independent estimates were obtained with the hybrid method. Each calculation consisted of simulating fifty thousand particles with 0.5 cm spacing with a different random number seed. The sample variance,

$$\sigma_j^2=\frac{1}{N-1}\sum_{n=1}^{N}\left(F_{j,n}-\bar{F}_j\right)^2, \tag{26}$$

was computed at each spatial point *j* for both methods. The sum of the variances at each spatial point and the average computational time (sec), $\langle T\rangle$, were used to compute the figure of merit,

$$\langle FOM \rangle = \frac{1}{\left(\sum_{j=1}^{J} \sigma_j^2 \right) \langle T \rangle}. \tag{27}$$

Table I. Figure of merit comparison for calculation of test problem scalar flux.

Method	$\sum_{j=1}^{J} \sigma_j^2$	<T>	<FOM>
Monte Carlo	211.7	259.6	1.820E-5
Hybrid	90.1	335.7	3.305E-5

The hybrid method figure of merit is 82% higher than standard Monte Carlo for the test problem. The hybrid method therefore offers a significant advantage in computational cost over Monte Carlo.

However, it should be noted that the hybrid method introduces spatial truncation error [Eqs. (18) and (22)] that is not present in standard Monte Carlo. In problems with a smoothly varying solution, these errors are insignificant compared to the statistical errors. However, when the solution is discontinuous or varies rapidly, care must be taken to discretize the problem appropriately.

4.2. Comparison with Standard Deterministic Methods

We compared the multigroup discrete ordinates (MGSN) method with the hybrid method for calculating the scalar flux and capture rate in the test problem. The benchmark solution was computed with Monte Carlo. The default grid spacing is 0.5 cm.

4.2.1. Description of transport effects

The spatially-averaged core and reflector spectra for the test problem were obtained with a benchmark Monte Carlo simulation and plotted in Fig. 2.

The differences in the two spectra are caused mainly by the cross section resonances. In the test problem, the flux near the interface has a spectrum between these two spectra and is strongly dependent on angle. For example, the energy spectrum of the neutrons located just inside the reflector near the interface and traveling with $\mu > 0$ is similar to the energy spectrum of the core. At the same spatial location, the spectrum of neutrons traveling with $\mu < 0$ is similar to the spectrum in the reflector.

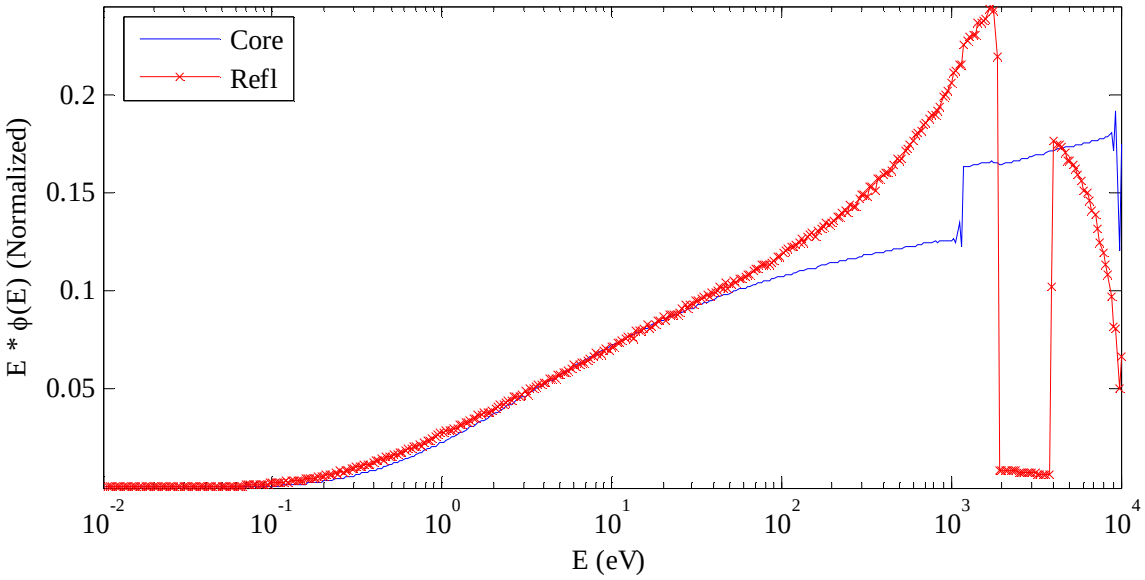

Figure 2. Core and reflector spectra for the test problem.

These directional spectral differences are not captured with the multigroup approximation, which assumes the same spectrum for neutrons traveling in all directions. We show here that multigroup methods do not perform well near the interface unless many groups are used, as was observed by Aliberti and Lebrat [1,2].

4.2.2. Multigroup cross section generation

An infinite medium Monte Carlo calculation was performed for each material (core and reflector) to compute the fine group spectrum and fine group cross sections. Multigroup cross sections were defined by weighting the continuous energy cross section with the spectrum (the conventional multigroup definition). An equal lethargy group structure was used, with 500 groups from 1 to 10 keV, and one additional group from 0 to 1 eV. The resulting 501-group cross sections were collapsed to 11, 21, 51, 101, and 251 groups with the infinite medium spectrum. The coarse group structures all contain one group from 0 to 1 eV,. The remaining groups are equal lethargy from 1 eV to 10 keV.

Computing multigroup cross sections in this manner is consistent with conventional methods. However, using the infinite medium spectrum to collapse cross sections rather than the true spectrum contributes error to the multigroup approximation. In future work we will isolate the effects of the collapsing with angularly-independent spectra from the effects of using spatially-independent spectra.

4.2.3. Scalar flux numerical results

The scalar flux for the test problem was computed using MGSN (S_{16} quadrature) and the hybrid method. The results are shown in Fig. 3.

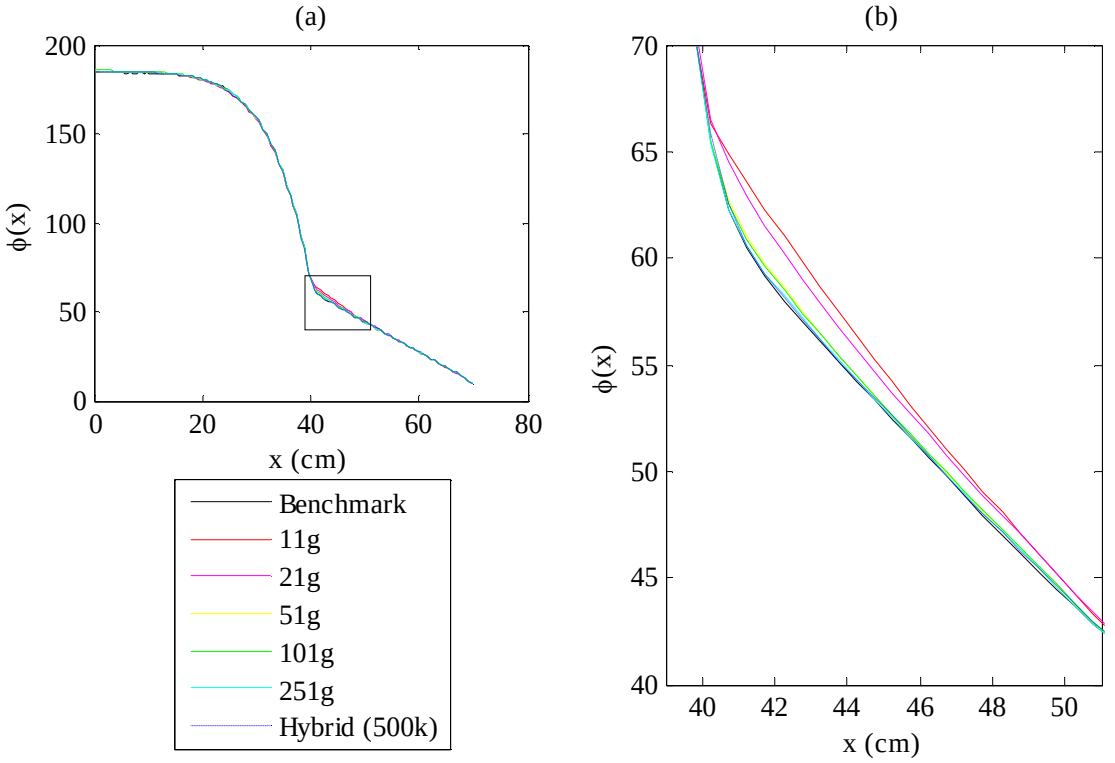

Figure 3. MGSN and hybrid scalar flux results for (a) slab, and (b) interface region.

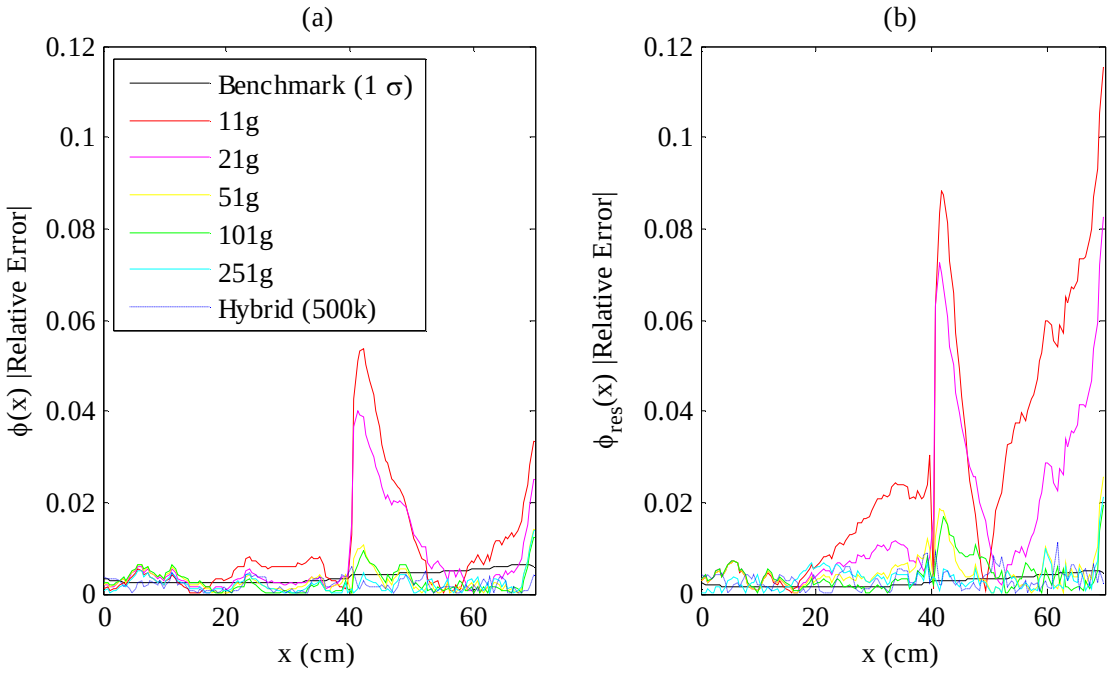

Figure 4. MGSN and hybrid relative errors in (a) scalar flux, and (b) resonance group flux.

The hybrid calculation performed very well in all parts of the problem. As the number of particles increased, the hybrid result improved (only the N=500K result is shown). The MGSN method performed well away from material interfaces but poorly near them. The MGSN results approached the benchmark solution as the group structure was refined, confirming that the multigroup approximation is the origin of error.

Since the spectral effects occur mostly in the resonance range, we divided the energy range into two groups, referred to as the *resonance group* (630.957 eV to 10 keV) and the *non-resonance group* (0 to 630.957 eV). As expected, the MGSN errors were more severe within the resonance group. The error in the total scalar flux (Fig. 4a) is less than that in the resonance component of the scalar flux (Fig. 4b).

Figs. 3 and 4 show that a 251 group structure is required to reduce the error near the interface and vacuum boundary to the benchmark uncertainty. This is an important finding: the one-group hybrid method performs at the same level as the 251 group structure by incorporating directional and spatial information. It should be noted that both 51g and 101g perform reasonably well but still exhibit the characteristic errors at the interface and vacuum boundary, with errors up to 2%.

4.2.4. Capture rate numerical results

To obtain the MGSN capture rates, the MGSN group scalar flux data was post-processed with corresponding group capture cross sections. The resonance capture rate and errors are shown in Figs. 5 and 6.

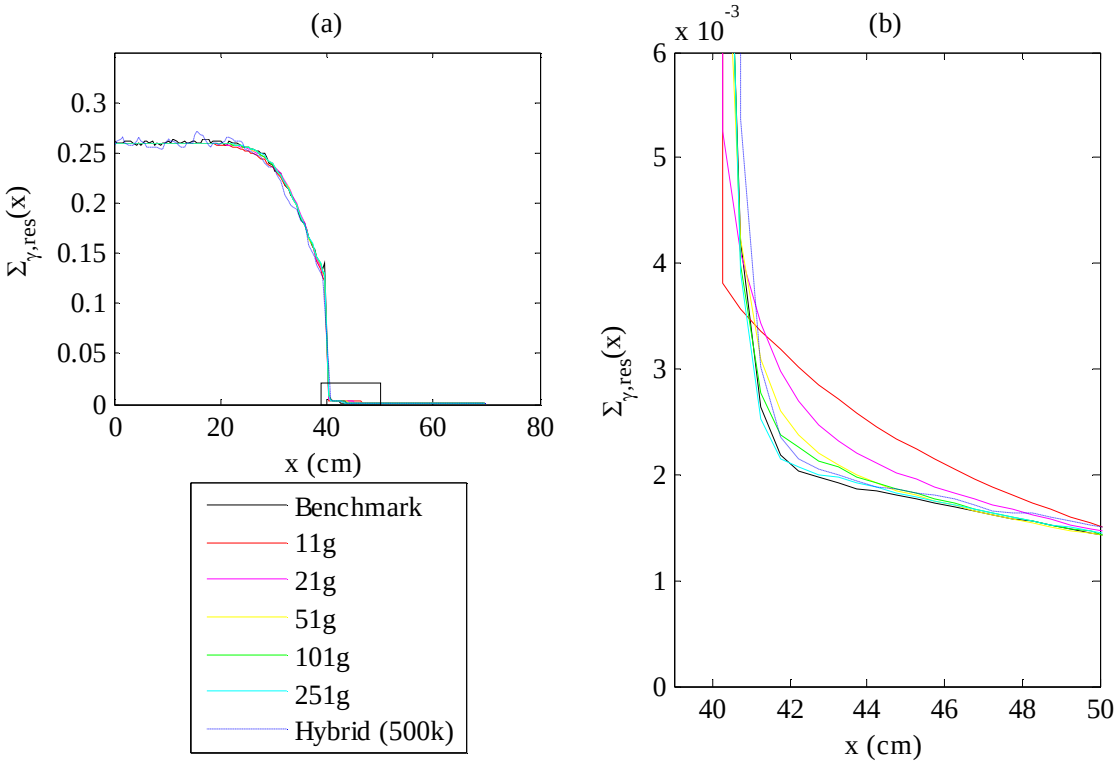

Figure 5. MGSN and hybrid resonance capture rates for (a) slab, and (b) interface region.

The resonance capture rate results are similar to the scalar flux results, except that large errors are observed in all methods at the interface. These errors are due to spatial truncation error rather than transport effects, since the solution changes rapidly and a coarse grid was used. Also, due to the resonances in this energy group, the hybrid method yields a higher variance results for the capture rate than the scalar flux. The variance can be suppressed by running more particles. Methods for suppressing the truncation error are discussed next.

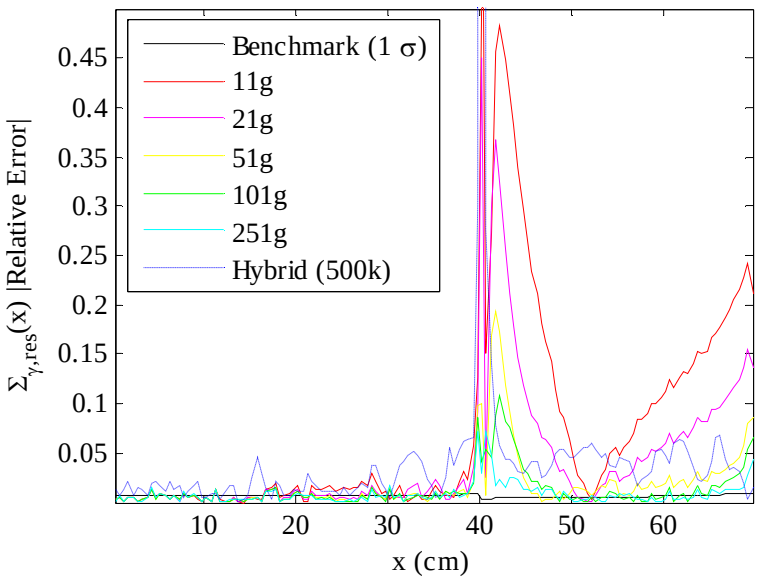

Figure 6. MGSN and hybrid relative errors in resonance capture rate.

The true capture rate is discontinuous and changes rapidly near the interface, where the function $f(x,E)$ is discontinuous. Due to the rapid solution change, significant spatial truncation error was observed in the hybrid solution when a coarse grid (0.5 cm) was used. The same error was also observed in the MGSN solution defined on the same grid. To decrease the error in the hybrid method, two techniques were used. The first technique was refinement of the spatial grid near the interface. The second technique was computation of the hybrid solution using the two spatially independent, continuous functions $f_{core}(x,E)=\Sigma_\gamma^{core}(E)$ and $f_{refl}(x,E)=\Sigma_\gamma^{refl}(E)$ to obtain $F_{core}(x)$ and $F_{refl}(x)$. This requires solving two low-order problems, but the necessary functionals are all obtained from just Monte Carlo run. Since the low-order problems are inexpensive, solving two of them (rather than one) adds very little overhead. The final solution is the piecewise function

$$F_{CF}(x)=\begin{cases}F_{core}(x), & x\in core\\ F_{refl}(x), & x\in reflector.\end{cases} \tag{28}$$

The *continuous function (CF)* method proved to be much more effective than simply refining the grid. However, using both methods in tandem produced the best results. Figure 7 and Table II show the results of using the regular hybrid method (with discontinuous $f(x,E)$) compared to the continuous function method for two different spatial grids.

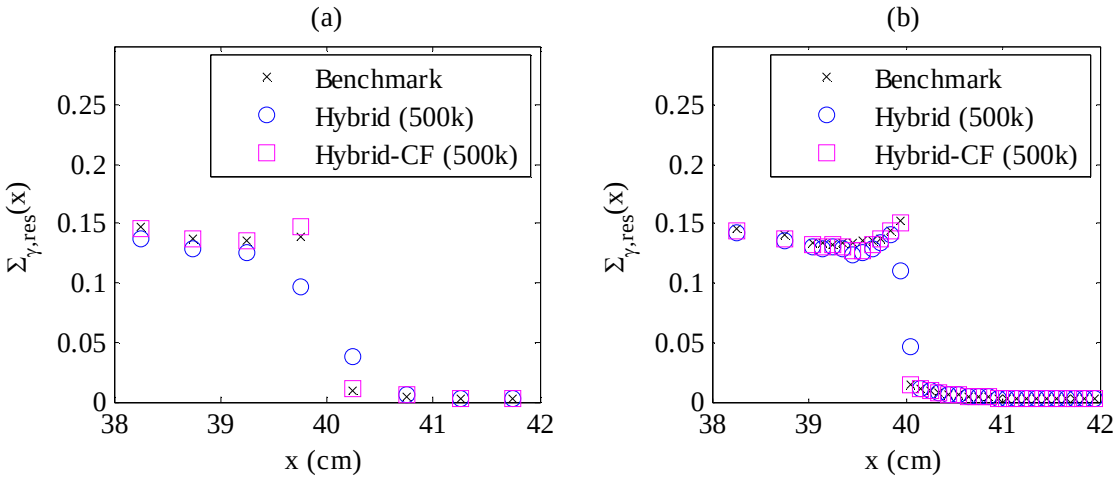

Figure 7. Hybrid resonance capture rate near interface: comparison of CF hybrid and ordinary hybrid methods on (a) coarse grid, and (b) fine grid.

Table II. Summary of spatial truncation error suppression techniques for hybrid method resonance capture rate calculation.

Method	Grid	Interface Max. Rel. Error
Regular	Coarse (dx=0.5)	292%
Regular	Fine (dx=0.1 near int.)	235%
CF	Coarse (dx=0.5)	23%
CF	Fine (dx=0.1 near int.)	2%

Use of the continuous function technique with a fine spatial grid suppressed the truncation error to within stochastic uncertainties. Therefore, the hybrid method is capable of handling discontinuous and rapidly changing solutions.

5. CONCLUSIONS

We have developed a hybrid method for accurately and efficiently solving difficult transport problems. The method consists of collapsing the transport equation in angle, energy, and space with only a small spatial truncation error. It should be noted that although the numerical results here were generated using the diamond difference scheme, the hybrid method does not require

the use of this specific approximation. The collapsing process produces cross section-like functionals that can be accurately computed by Monte Carlo.

For the test problem, the hybrid method results agree with the benchmark Monte Carlo solution, and have less variance than computation time-equivalent Monte Carlo solutions. In addition, the hybrid method is more accurate than conventional multigroup discrete ordinates methods for problems exhibiting transport effects. The hybrid method can also handle problems with discontinuous and rapidly varying solutions by refining the spatial grid and using the continuous function technique described. In addition, the hybrid method eliminates possible sources of error such as improper choice of energy group boundaries and insufficient number of discrete ordinates directions. Finally, because the hybrid method has no approximation in angle, it may be advantageous for solving problems where discrete ordinates calculations exhibit undesirable ray effects.

In the future we plan to extend this work to handle eigenvalue problems, anisotropic scattering, and more general geometries. We also plan to further investigate the differences between the new method and various multigroup methods by generating the multigroup cross sections in different ways. In addition, we will explore ways to reduce the variance of the hybrid result by studying alternative computations of the functional quantities.

ACKNOWLEDGMENTS

This work was funded in part by a United States Department of Energy Nuclear Engineering and Health Physics Fellowship.

REFERENCES

1. G. Aliberti, G. Palmiotti, M. Salvatores, J.F. Lebrat, J. Tommasi, R. Jacqmin, "Methodologies for Treatment of Spectral Effects at Core-Reflector Interfaces in Fast Neutron Systems," *Proceedings of International Conference on the Physics of Reactors*, Chicago, Illinois, April 25-29, 2004.
2. J.F. Lebrat, R. Jacqmin, F. Gabrielli, M. Carta, V. Peluso, G. Buzzi, G. Bianchini, A. D'Angelo, G. Aliberti, G. Palmiotti, "Fast Reactor Core-Reflector Interface Effects Revisited," *Proceedings of International Conference on the Physics of Reactors*, Seoul, Korea, October 7-10, 2002.
3. R. Corcuera and A. Khairallah, "Fine Neutron-Spectrum Effects on Spatial Calculations for Fast-Reactor Design," *Nucl. Sci. and Eng.*, **53**, pp. 420-435 (1974).
4. D. Meneghetti and K.E. Phillips, "Fine-Spectral Interface Effects of Resonance Scattering Upon Multigroup Cross Section Averaging," *J. Nucl. Eng.*, **24**, pp. 509-524 (1970).
5. H.L. Hanshaw, A. Haghighat, and J.C. Wagner, "Multigroup Cross-Section Generation with Spatial and Angular Adjoint Weighting", *Trans. Amer. Nucl. Soc.*, San Francisco, California, Oct 29-Nov 2, 1995, Vol. 73, pp. 175-177 (1995).
6. H.L. Hanshaw, "Multigroup Cross Section Generation with Spatial and Angular Adjoint Weighting," MS Thesis, Pennsylvania State University, (1995).
7. L. Roberts and D.Y. Anistratov, "Nonlinear Weighted Flux Methods for Particle Transport Problems," *Transp. Theory Stat. Phys.*, **36**, 7, pp. 589-608 (2007).

APPENDIX A

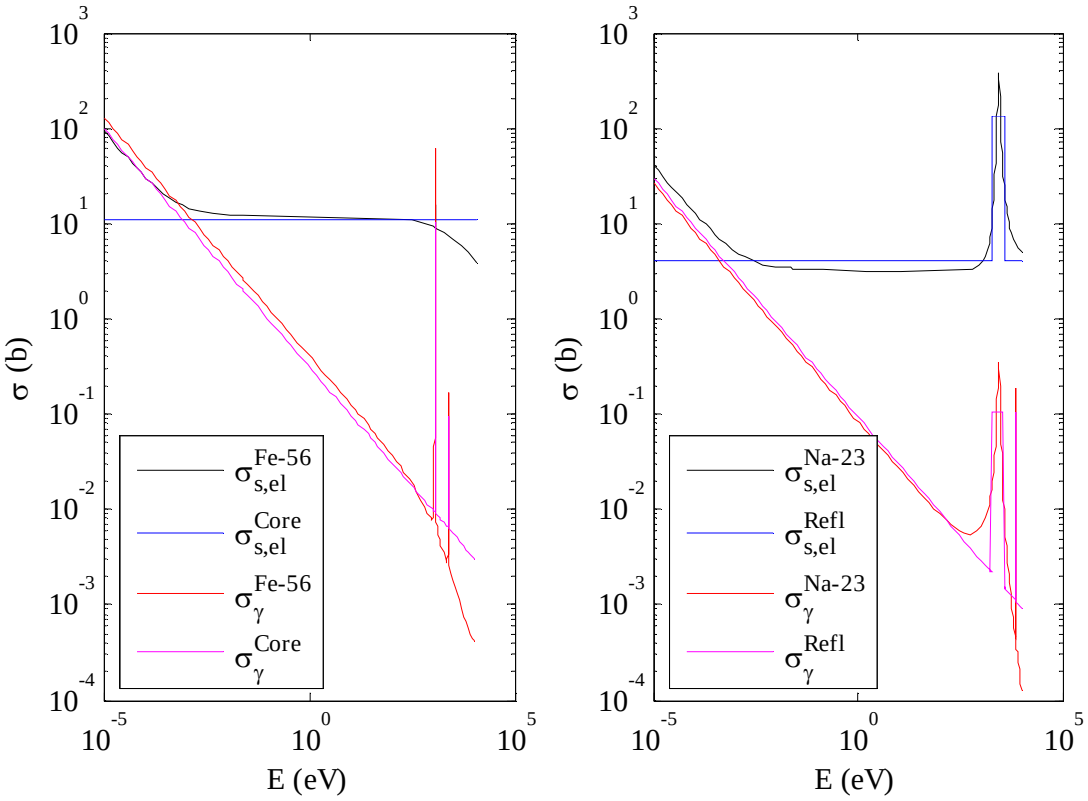

Figure A-1. Cross sections used for core and reflector compared with ENDF/B-VII.0 data for Fe-56 and Na-23.

Table A-I. Material properties of test problem.

Region	Atomic Number	Number Density (#/barn-cm)
I (Core)	56	0.0848
II (Reflector)	23	0.0254